Wall-shear-stress measurement and characterization at high Reynolds numbers

By T.M. Jaroslawski, F. Cabrera-Booman, J.M.O. Massey AND B.J. McKeon

Wall-shear stress is a fundamental quantity in turbulent boundary layers; it sets skin-friction drag and power expenditure, governs momentum and heat transfer at the wall, and underpins validation of near-wall turbulence models. This brief reports time-resolved wall-shear-stress measurements at high Reynolds number in Stanford's pressurized wind tunnel, quantifies the Reynolds number dependence of the wall-shear-stress spectrum, and isolates sensor-footprint filtering through comparison with numerical simulation.

1. Introduction

Many vehicles of practical interest operate at high Reynolds numbers, where turbulent boundary layers exhibit dynamics that differ fundamentally from those at low Reynolds numbers. In particular, very large scale motions (VLSMs) become increasingly energetic and may influence wall-shear-stress fluctuations. This behavior challenges current models, which rely heavily on low-Reynolds-number data and fail to accurately capture the contribution of these large scales.

In wall-bounded turbulence, streamwise velocity fluctuations originate from two primary sources: the small-scale motions of the near-wall cycle and the imprint or modulation of large-scale motions (LSMs) and VLSMs from the outer layer. As the Reynolds number increases, the relative importance of these outer layer–induced, low-frequency contributions grows, altering spectra, intermittency, and scaling (Smits *et al.* 2011).

Studies have shown that the superposition of large-scale signatures leaves a measurable imprint on the wall-shear stress τ_w (Metzger & Klewicki 2001; Mathis *et al.* 2009, 2013; Schlatter & Örlü 2010). Specifically, low-frequency wall-shear-stress fluctuations reflect the footprint of outer layer motions, which Bradshaw (1967) and Deshpande *et al.* (2025) propose to be inactive; that is, they contribute negligibly to local Reynolds shear stress and momentum transfer while strongly manifesting in streamwise-velocity energy and modulating near-wall dynamics.

Despite significant advances, the dynamics of low-frequency, subconvective wall-shear-stress fluctuations remain insufficiently characterized, particularly at high Reynolds numbers, where their influence becomes dominant. These motions represent the direct wall imprint of large-scale turbulence, drive intermittency in skin friction, and hinder the development of accurate predictive models and control strategies. Experimental data remain scarce, especially from direct time-resolved measurements of τ_w, limiting our ability to fully assess their role.

In this brief, we employ time-resolved wall-shear-stress sensors to resolve the low-frequency content of τ_w across a range of Reynolds numbers. The measurements quantify the contribution of subconvective motions to wall-shear-stress variability. These results underscore the importance of understanding the physical mechanisms for measurement

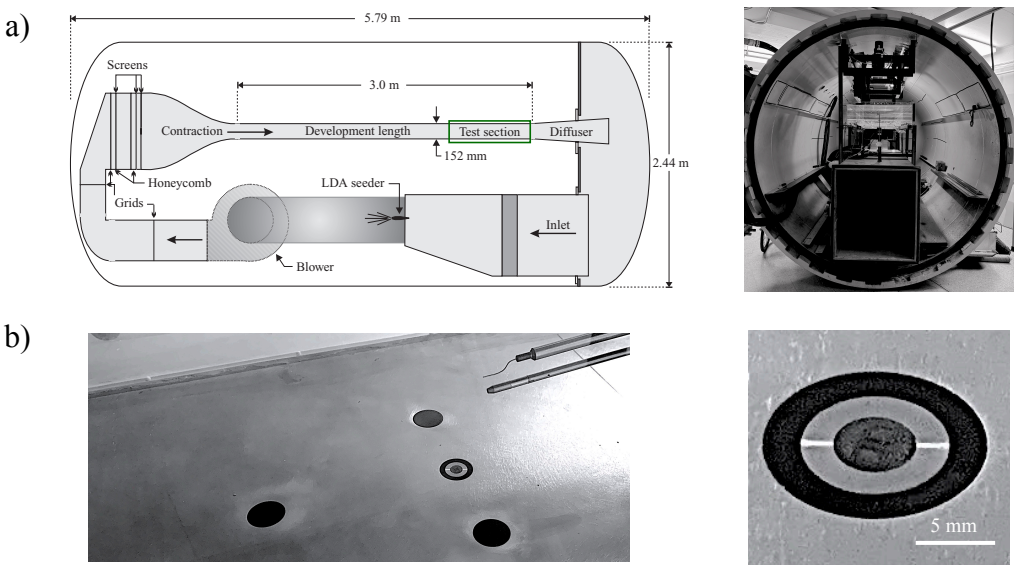

FIGURE 1. (a) Schematic (adapted from De Graaff & Eaton 2000) (left) and photograph of the facility with the test-section door open (right). (b) Inset of the test section (left) and close-up view of the wall-shear-stress sensor (right).

limitations of wall-shear stress at high Reynolds numbers, as predictive models cannot be refined without accurately characterizing the underlying dynamics.

2. The approach

2.1. *Pressurized wind tunnel experiments*

Figure 1(a) presents a schematic of the pressurized wind tunnel, which was recently refurbished (De Graaff & Eaton 2000; Cabrera-Booman *et al.* 2024). The facility attains high Reynolds numbers by enclosing the entire flow circuit within a pressure vessel and operating at elevated absolute pressure. Increasing the pressure raises the air density and reduces the value of the kinematic viscosity. This enables high Reynolds numbers (up to friction Reynolds numbers on the order of 10^4), defined as $Re_\tau \equiv u_\tau \delta_{BL}/\nu$, where δ_{BL} is the boundary layer thickness, u_τ is the friction velocity, and ν is the fluid's kinematic viscosity at modest development lengths, with thinner boundary layers and relatively low bulk velocities. Details of the tunnel geometry and ancillary systems are omitted here; we focus only on aspects relevant to the current experiment. For further information, the reader is referred to De Graaff & Eaton (2000).

The working section measures 3.0 × 0.15 × 0.71 m (length × height × width). The lower wall incorporates a removable transparent plate with an inset region (0.95 × 0.30 m) accommodating a 6-mm-thick aluminum plate flush-mounted to the wall. Precision-drilled holes and associated flush-mounted insets/plugs in the inset plate allow for flush-mounted pressure and shear-stress instrumentation (Figure 1(b)). The upstream step height at the leading edge of the inset was measured to be less than 200 μm under atmospheric conditions, and measurement stations were placed more than 2,500 step heights downstream to eliminate any influence of the step.

Freestream velocity was determined using a static-pressure Pitot tube connected to a

manometer, positioned approximately at midchannel 2.6 m downstream of the trip. Stable operating velocities ranged from 3 to 14 m/s. Baseline flow quality and turbulence levels were validated in prior work using hot-wire anemometry; here we focus on wall-shear-stress measurements.

2.2. *Time-resolved wall-shear-stress measurements*

Wall-shear stress, τ_w, was measured using flush-mounted capacitive sensors (IC2 CS-0510) located on the spanwise centerline approximately 2.5 m downstream of the trip. Sensors were installed to tight tolerances, with a maximum step between the sensing surface and the wall of 25 μm; the manufacturer specifies <25 μm on the sensitive element itself, which at the highest Reynolds numbers corresponds to about 5 viscous units ($y^+ \equiv y\,u_\tau/\nu$). Each sensing element has a 2.0 × 0.4 mm footprint, implying finite spatial averaging at the wall. The usable bandwidth is approximately 700 Hz. Signals were sampled at 5 kHz with an analog low-pass filter at 700 Hz. Acquisition durations spanned many large-eddy turnover times to ensure statistical convergence.

Flushness and orientation are critical. During development, we observed that small angular misalignment could introduce artifacts—most notably spurious negative τ_w and depressed mean/shear estimates—likely due to local flow disturbance over the element (possible microseparation; not confirmed). All results reported here were acquired with verified flushness and alignment within the stated tolerances.

2.2.1. *Uncertainty quantification*

We estimate the skin-friction coefficient via

$$C_f \;\equiv\; \frac{2\,\tau_w}{\rho\,U_\infty^2}$$

and propagate uncertainty from two independent sources: wall-shear sensor errors mapped into σ_{τ_w} and freestream condition uncertainties in ρ and U_∞. The density is modeled as an ideal gas,

$$\rho \;\equiv\; \frac{p}{RT},$$

with relative uncertainty

$$\frac{\sigma_\rho}{\rho} \;=\; \sqrt{\left(\frac{\sigma_p}{p}\right)^2 + \left(\frac{\sigma_T}{T}\right)^2}.$$

Wall-shear uncertainty aggregates independent sensor-side contributions in root sum square. The sensor resolution is $\mathrm{Res} = \mathrm{Res}_{\mathrm{mPa}} \times 10^{-3}$ (Pa), the integrated noise

$$\mathrm{Noise} \;=\; \frac{n_f\,\sqrt{f_b}}{S},$$

where n_f is the voltage noise density ($\mathrm{V}/\sqrt{\mathrm{Hz}}$), f_b is the effective measurement bandwidth (Hz), and S is the sensor sensitivity (V/Pa); the DC accuracy (calibration/bias) DCacc (either measured directly or taken as $\mathrm{DCacc} = \mathrm{DCacc}_{\mathrm{spec}} \times \mathrm{FS}$), where FS is full scale; and the temperature-induced offset drift

$$\mathrm{Temp} \;=\; \alpha_T\,\mathrm{FS}\,|\Delta T|,$$

where α_T is the drift coefficient (fraction of full scale per degree Celsius), FS wall-shear

(Pa). ΔT is the temperature drift in the experiment. These combine as

$\sigma_{\tau_w} = \sqrt{\mathrm{Res}^2 + \mathrm{Noise}^2 + \mathrm{DCacc}^2 + \mathrm{Temp}^2}$; $\dfrac{\sigma_{\tau_w}}{\tau_w}$ is the relative wall-shear uncertainty.

The sensor-only contribution to the skin-friction uncertainty is

$$\delta C_{f,\mathrm{sensor}} = \frac{2}{\rho U_\infty^2}\,\sigma_{\tau_w}, \qquad \frac{\delta C_{f,\mathrm{sensor}}}{C_f} = \frac{\sigma_{\tau_w}}{\tau_w}.$$

Freestream contributions enter through ρ and U_∞, yielding

$$\frac{\delta C_{f,\mathrm{freestream}}}{C_f} = \sqrt{\left(\frac{\sigma_\rho}{\rho}\right)^2 + \left(2\,\frac{\sigma_U}{U_\infty}\right)^2}, \qquad \delta C_{f,\mathrm{freestream}} = C_f \sqrt{\left(\frac{\sigma_\rho}{\rho}\right)^2 + \left(2\,\frac{\sigma_U}{U_\infty}\right)^2}.$$

Assuming independence between sensor and freestream sources, the total uncertainty is

$$\delta C_{f,\mathrm{tot}} = \sqrt{\delta C_{f,\mathrm{sensor}}^2 + \delta C_{f,\mathrm{freestream}}^2}; \qquad \frac{\delta C_{f,\mathrm{tot}}}{C_f} = \frac{1}{C_f}\sqrt{\delta C_{f,\mathrm{sensor}}^2 + \delta C_{f,\mathrm{freestream}}^2}.$$

The coefficients in the relative error terms follow from logarithmic differentiation of C_f: τ_w and ρ appear to the first power, while U_∞ appears squared.

We also report the friction velocity,

$$u_\tau = \sqrt{\frac{\tau_w}{\rho}},$$

with relative and absolute uncertainties

$$\frac{\sigma_{u_\tau}}{u_\tau} = \sqrt{\left(\tfrac{1}{2}\,\tfrac{\sigma_{\tau_w}}{\tau_w}\right)^2 + \left(\tfrac{1}{2}\,\tfrac{\sigma_\rho}{\rho}\right)^2}, \qquad \sigma_{u_\tau} = u_\tau \sqrt{\left(\tfrac{1}{2}\,\tfrac{\sigma_{\tau_w}}{\tau_w}\right)^2 + \left(\tfrac{1}{2}\,\tfrac{\sigma_\rho}{\rho}\right)^2}.$$

The factors of $1/2$ arise because u_τ contains square roots of both τ_w and ρ.

To propagate viscosity from temperature via Sutherland's law, we write

$$\mu = \mu_{\mathrm{ref}} \left(\frac{T}{T_{\mathrm{ref}}}\right)^{3/2} \frac{T_{\mathrm{ref}} + S}{T + S}, \qquad \frac{\mathrm{d}\ln\mu}{\mathrm{d}T} = \frac{3}{2T} - \frac{1}{T+S}, \qquad \frac{\sigma_\mu}{\mu} = \left|\frac{\mathrm{d}\ln\mu}{\mathrm{d}T}\right| \sigma_T.$$

With kinematic viscosity $\nu = \mu/\rho$, we obtain

$$\frac{\sigma_\nu}{\nu} = \sqrt{\left(\frac{\sigma_\mu}{\mu}\right)^2 + \left(\frac{\sigma_\rho}{\rho}\right)^2}.$$

For Re_τ,

$$\frac{\sigma_{Re_\tau}}{Re_\tau} = \sqrt{\left(\frac{\sigma_{u_\tau}}{u_\tau}\right)^2 + \left(\frac{\sigma_\delta}{\delta_{\mathrm{BL}}}\right)^2 + \left(\frac{\sigma_\nu}{\nu}\right)^2}.$$

For the normalized turbulent wall-shear fluctuation $\tau_w'^+$, when the sample count is large and bias is negligible, we use the approximation

$$\frac{\delta(\tau_w'^+)}{\tau_w'^+} \approx \frac{\sigma_{\tau_w}}{\tau_w}.$$

Throughout, we assume small, independent uncertainties and first-order (linear) propagation; noise is integrated over the effective measurement bandwidth, and temperature drift is modeled as an offset proportional to full scale per degree Celsius.

2.3. *Direct numerical simulation surrogate for sensor footprint effects on τ_w*

A wall-shear sensor with finite physical length acts as a spatial low-pass filter, attenuating high-frequency energy. As the Reynolds number increases, viscous scales shrink, so a fixed-size sensor filters a larger fraction of near-wall motions. We quantify this finite-footprint filtering in direct numerical simulations (DNS) by applying streamwise spatial filters matched to the sensor footprint and varying their length in wall units to emulate increasing Reynolds numbers.

We use channel-flow DNS data from Huang *et al.* (2025) and Toedtli *et al.* (2025), generated with the solver presented by Flores & Jimenez (2006). The channel half-height is denoted by h; the domain size is $4\pi h \times 2\pi h$; and the friction Reynolds number is approximately 551. The solver employs spectral discretization in the streamwise (x) and spanwise (z) directions, computes nonlinear terms in physical space with 2/3 dealiasing, and uses a compact finite-difference scheme in the wall-normal (y) direction with $N_y = 272$ points.

3. Results

3.1. *Mean skin friction versus Reynolds number*

Figure 2 presents the mean skin-friction coefficient, C_f, as a function of the friction Reynolds number, Re_τ, derived from our direct measurements of wall-shear stress. Data span a range of speeds and freestream pressures. For reference, the plot includes a spread of empirical correlations in the literature (namely, the 1/4- and 1/7-power laws) alongside results from De Graaff & Eaton (2000), in which the wall-shear stress, τ_w, was inferred by least-squares fitting of the logarithmic law to the mean velocity profile over the interval $50 \leq y^+$ and $y/\delta \leq 0.2$. The present measurements are consistent with De Graaff & Eaton (2000) within the stated experimental uncertainty and reproduce the same trend: the effective exponent in a power-law representation decreases with increasing Re_τ, implying that fixed-exponent power-law estimates of C_f are reliable only at low Reynolds numbers.

The relatively large uncertainties observed at low Reynolds numbers are anticipated. Under low freestream pressure, the physical wall-shear forces are small, placing the shear-stress sensor near the lower end of its dynamic range. In this regime, resolution and broadband noise constitute a larger fraction of the signal, and temperature-induced offset drift is less effectively suppressed, which degrades the signal-to-noise ratio. Consequently, the relative uncertainty in τ_w—and, by propagation, in C_f—is elevated at low Re_τ.

3.2. *Spectral content of the wall-shear-stress fluctuations*

Here we present wall-shear-stress spectra. The Reynolds number is controlled by adjusting freestream velocity U_∞ and pressure (hence density ρ) at near-constant temperature; for iso-Reynolds-number operation, U_∞ and ρ are covaried to keep $Re = \rho U_\infty L/\mu$ constant. Increasing pressure raises ρ and lowers $\nu = \mu/\rho$.

3.2.1. *Iso-Reynolds-number experiments*

Figure 3 shows the premultiplied wall-shear-stress spectrum, $f\,\phi^+_{\tau_w\tau_w}(f)$, plotted against the inner-scaled period $T^+ = 1/f^+$, where $f^+ = f\,\nu/u_\tau^2$. We compare two friction Reynolds numbers, $Re_\tau \approx 1200$ and $Re_\tau \approx 6000$, and include DNS data from Eitel-Amor *et al.* (2014) for reference. The $Re_\tau \approx 1200$ condition was reproduced under iso-Re_τ con-

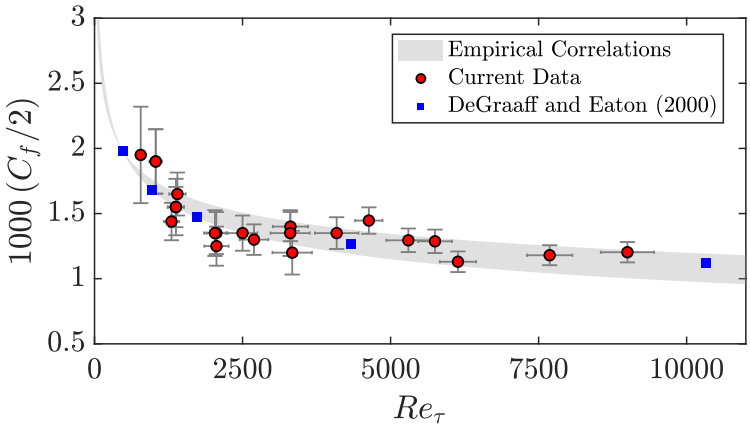

FIGURE 2. Mean skin-friction coefficient versus the friction Reynolds number. Experimental results are plotted across a range of speeds and freestream pressures.

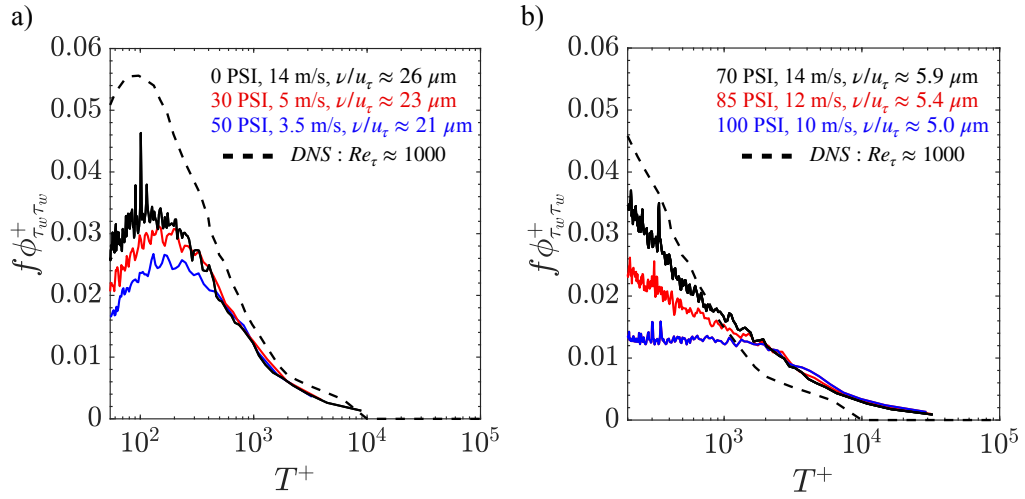

FIGURE 3. Iso-Reynolds-number experiments obtained under three different freestream conditions. (a) $Re_\tau \approx 1200$. (b) $Re_\tau \approx 6000$. The dashed line represents data obtained from Eitel-Amor *et al.* (2014).

ditions by reducing the freestream velocity while increasing the test-section pressure, yielding the same Re_τ as at atmospheric pressure with $U \approx 14$ m/s.

Two features emerge. First, the spectral energy attenuates at $T^+ \lesssim 100$, attributable to spatial averaging by the finite-sensing element (∼0.4 mm), which increasingly underresolves the shrinking viscous scales (discussed further in Section 3.2.3). Second, the spectra collapse at large T^+ (low frequencies) across all iso-Re_τ realizations, consistent with DNS and indicating that spatial filtering does not contaminate the larger timescales to the first order. At $Re_\tau \approx 6000$, we observe the same spatial filtering attenuation at $T^+ \lesssim 100$. At large T^+, the spectra again collapse and exhibit more energy than the low-Re DNS reference; this topic is discussed in the next section.

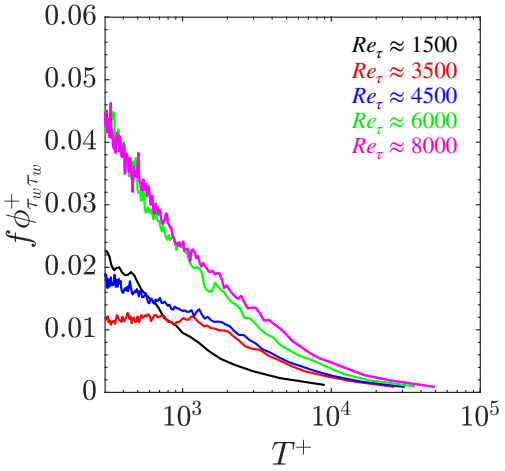

FIGURE 4. Premultiplied energy spectra of the wall-shear stress, τ_w, for different Re_τ.

3.2.2. *Effects of high Reynolds number on the wall-shear-stress spectrum*

Figure 4 presents premultiplied spectra of wall-shear-stress fluctuations over friction Reynolds numbers from $Re_\tau \approx 1500$ to $Re_\tau \approx 8000$. As Re_τ increases, the spectra exhibit a systematic rise in energy at large T^+, indicating strengthened low-frequency fluctuations in τ_w associated with the footprint of outer layer motions (Metzger & Klewicki 2001; Mathis *et al.* 2013; Deshpande *et al.* 2025). In this regime, subconvective signatures emerge—structures whose streamwise extents and apparent convection velocities yield periods far exceeding those of the near-wall cycle. These motions enhance long-period spectral content and promote intermittency in τ_w, consistent with intensified outer–inner interactions at high Re_τ. As discussed for the iso-Reynolds-number experiments, we also observe attenuation of the spectra at low T^+.

3.2.3. *Spatial filtering of τ_w from direct numerical simulations*

Next, we use DNS of channel flow at $Re_\tau = 550$ to further validate the observed filtering phenomenon. Specifically, we analyze the spectral content of τ_w after applying spatial filters corresponding to the sensing element size, expressed in wall units as l^+_{filt}. By systematically increasing l^+_{filt}, we approximate the effect of increasing the Reynolds number, since higher Re_τ leads to smaller viscous scales relative to a fixed physical sensor size.

Figure 5(a) presents the two-dimensional spectrogram of wall-shear stress; vertical dashed lines indicate the scales expected to be attenuated at experimental Reynolds numbers. The corresponding premultiplied energy spectra are shown in Figure 5(b). Increasing the effective Reynolds number—approximated here by increasing l^+_{filt}—yields behavior consistent with the experiments (Figure 5(b)): a systematic decrease in spectral energy associated with the near-wall cycle, including a slight rightward shift of the spectral peak. At larger periods (large T^+), the spectra remain relatively unaffected, except at the highest effective Reynolds numbers, where the sensor footprint becomes comparable to the channel half-height.

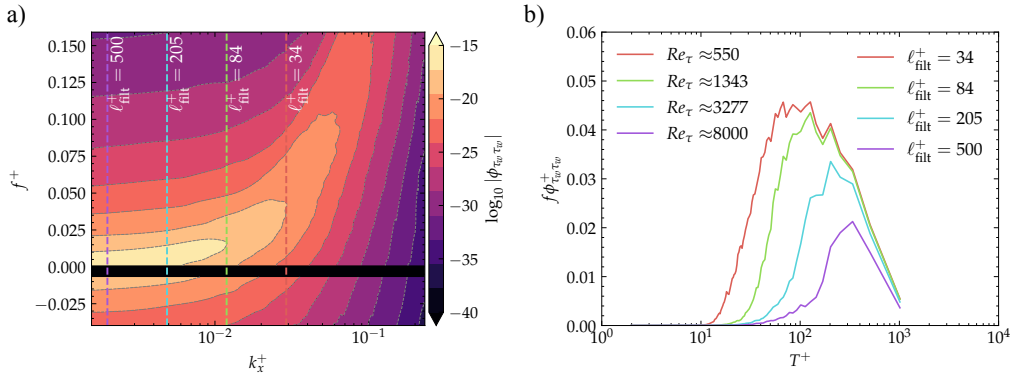

FIGURE 5. Inner-scaled wall-shear-stress spectra from DNS at $Re_\tau = 550$. (a) Spectrogram of wall-shear stress with theoretical filter cutoffs overlaid. k_x^+ is the inner-scaled streamwise wavenumber. (b) Premultiplied energy spectra of the DNS data after application of the theoretical effective spatial filter at the corresponding Reynolds number. The DC component has been removed, as indicated by the black line.

4. Conclusions and future work

We presented experiments on time-resolved wall-shear-stress measurements and characterized the mean skin-friction coefficient. We analyzed spatial filtering caused by the finite-sensing element, showing that small-scale structures are attenuated by the sensor whereas large-scale motions are largely unaffected. We corroborated these findings using synthetic sensor modeling, which consisted of applying analogous spatial filtering to DNS data. Studying these effects under iso-Re_τ conditions isolates spatial filtering influences from Reynolds number variation. We also examined the Reynolds number dependence of the wall-shear-stress spectra and found that increasing Re_τ elevates low-frequency energy. Building on this finding, we are developing a correction framework that compensates for attenuation and reconstructs the missing spectral content, exploiting the universality of the wall-shear-stress spectrum at low T^+. A complementary model, following Gustenyov *et al.* (2025) and Massey *et al.* (2025), incorporates both inner- and outer-scale dynamics to capture the full structure of the wall-shear-stress spectrum.

Acknowledgments

The authors acknowledge Alexander Smits, Ivan Marusic, Marcus Hultmark, Vijaya Gudla, Kyle Devlin, Liuyang Ding, and Joseph Klewicki for their collaboration in the broader context of the SAPPHIRE project. Support from DARPA under award HR0011-24-9-0465 is gratefully acknowledged.

REFERENCES

BRADSHAW, P. 1967 'Inactive' motion and pressure fluctuations in turbulent boundary layers. *J. Fluid Mech.* **30**, 241–258.

CABRERA-BOOMAN, F., MASSEY, J. & MCKEON, B. J. 2024 High-Reynolds-number and low-Mach-number wind tunnel at Stanford University. *Annual Research Briefs,* Center for Turbulence Research, Stanford University, pp. 203–210.

DE GRAAFF, D. B. & EATON, J. K. 2000 Reynolds-number scaling of the flat-plate turbulent boundary layer. *J. Fluid Mech.* **422**, 319–346.

DESHPANDE, R., VINUESA, R., KLEWICKI, J. & MARUSIC, I. 2025 Active and inactive

contributions to the wall pressure and wall-shear stress in turbulent boundary layers. *J. Fluid Mech.* **1003**, A24.

Eitel-Amor, G., Örlü, R. & Schlatter, P. 2014 Simulation and validation of a spatially evolving turbulent boundary layer up to Re_θ= 8300. *Int. J. Heat Fluid Flow* **47**, 57–69.

Flores, O. & Jimenez, J. 2006 Effect of wall-boundary disturbances on turbulent channel flows. *J. Fluid Mech.* **566**, 357–376.

Gustenyov, N., Bailey, S. C. & Smits, A. J. 2025 A model spectrum for turbulent wall-bounded flow. *J. Fluid Mech.* **1016**, A23.

Huang, Y., Toedtli, S., Chini, G. & McKeon, B. J. 2025 Spatio-temporal characterization of nonlinear forcing and response in turbulent channel flow. arXiv:2503.06915 [physics.flu-dyn].

Massey, J. M., Smits, A. J. & McKeon, B. J. 2025 Eddy population based model for the wall-pressure spectrum at high Reynolds number. arXiv:2507.23098 [physics.flu-dyn] .

Mathis, R., Hutchins, N. & Marusic, I. 2009 Large-scale amplitude modulation of the small-scale structures in turbulent boundary layers. *J. Fluid Mech.* **628**, 311–337.

Mathis, R., Marusic, I., Chernyshenko, S. I. & Hutchins, N. 2013 Estimating wall-shear-stress fluctuations given an outer region input. *J. Fluid Mech.* **715**, 163–180.

Metzger, M. & Klewicki, J. 2001 A comparative study of near-wall turbulence in high and low Reynolds number boundary layers. *Phys. Fluids* **13**, 692–701.

Schlatter, P. & Örlü, R. 2010 Assessment of direct numerical simulation data of turbulent boundary layers. *J. Fluid Mech.* **659**, 116–126.

Smits, A. J., McKeon, B. J. & Marusic, I. 2011 High–Reynolds number wall turbulence. *Annu. Rev. Fluid Mech.* **43**, 353–375.

Toedtli, S., Leonard, A. & McKeon, B. 2025 Coupled dynamics of wall pressure and transpiration, with implications for the modelling of tailored surfaces and turbulent drag reduction. *J. Fluid Mech.* **1019**, A18.